Fast PolSAR Data Visualization and Classification Based on Huynen Canonical Decomposition

Dong, Li, Key Lab of Microwave Remote Sensing, Chinese Academy of Sciences, lidong@mirslab.cn, China
Yunhua, Zhang, Key Lab of Microwave Remote Sensing, Chinese Academy of Sciences, China

chinaXiv:201701.00023v1

Abstract

A scattering degree of preference parameter is developed from Huynen canonical dichotomy which displays superior classification ability over the scattering similarity parameter. A scattering hue parameter is then proposed and demonstrated to be of superiority compared with scattering alpha on description of scattering mechanism. A scattering saturation parameter is further defined and shows comparable to scattering entropy on description of scattering randomness. A Huynen dichotomy-based PolSAR data visualization scheme is finally obtained which not only works more efficient but also makes the results look better than that from H/alpha.

1 Introduction

It is unbiased to say that it is Dr. J. R. Huynen pioneered the area of polarimetric target decomposition. In his dissertation on the phenomenological theory of radar target [1], Huynen formally developed the coherent and incoherent decompositions. The coherent one expresses the scattering matrix of a determined target in terms of several physical parameters, such as SPAN, orientation, and helicity, which was further extended for the well-used Cameron decomposition and Touzi decomposition [2]; while the incoherent one is also known as Huynen target dichotomy because it decomposes a random target scattering into the incoherent sum of an equivalent single target scattering and a remnant noisy *N*-target scattering [1]. This decomposition has clear physical significance because it prefers the real world of symmetry. However, it is not mathematically unique because there exist other target dichotomies, such as Holm-Barnes decomposition and Yang decomposition [2]. The contributions of Holm, Barnes, and Yang improve Huynen dichotomy significantly, but there is no unified criterion for us to select between them. A Huynen canonical dichotomy is developed and extended for a generalized dichotomy in [3]. The dichotomy can unify the existing Huynen-like target dichotomies and shows comparable decomposition and classification ability as the Cloude-Pottier decomposition [3]. This paper further focuses on Huynen canonical dichotomy. Our recent research shows that the dichotomy can provide a fast and better way to visualize and classify PolSAR data, as will be detailed as follows.

2 Huynen Canonical Dichotomy

We first give a concise introduction to Huynen canonical dichotomy. The original Huynen dichotomy behaves well on the symmetrically and regularly dominant radar target. For targets of complex non-symmetry and irregularity, however, it will fail. Huynen added that the attention should turn to *N*-target instead of single target in these cases [1]. But *N*-target is clearly defective because it cannot completely reserve the non-symmetric and irregular target information. By referring to wave dichotomy, it is found that there still exist two other target dichotomies [3]. The Pauli vectors (i.e. $\vec{k}_2$ and $\vec{k}_3$) of single targets extracted from them are shown in (1), where $\vec{k}_1$ is that extracted from Huynen dichotomy, and T_{ij} denotes the element of target coherency matrix [*T*].

$$\vec{k}_1 = \frac{1}{\sqrt{T_{11}}}\begin{bmatrix} T_{11} \\ T_{21} \\ T_{31} \end{bmatrix}, \vec{k}_2 = \frac{1}{\sqrt{T_{22}}}\begin{bmatrix} T_{12} \\ T_{22} \\ T_{32} \end{bmatrix}, \vec{k}_3 = \frac{1}{\sqrt{T_{33}}}\begin{bmatrix} T_{13} \\ T_{23} \\ T_{33} \end{bmatrix}. \quad (1)$$

Each column of [*T*] is just one of the Pauli vectors in (1) and is kept invariant to a dichotomy because they are reserved by dichotomies $\vec{k}_1$, $\vec{k}_2$ and $\vec{k}_3$, respectively [3]. The diagonal entries T_{11}, T_{22}, and T_{33} physically relate to target scattering of symmetry/regularity, irregularity, and non-symmetry, respectively, according to Huynen phenomenological theory [1]. They also denote the scattering similarity between [*T*] and the canonical scatterers, i.e. the sphere, dihedral, and volume scatterer, respectively [4]. Thus the parameter invariance may show the scattering preference of each dichotomy. This can be clearly demonstrated in Fig. 1 on the AIRSAR data of San Francisco using the Pauli pseudo-colour illustration. Comparing with the original image shown in Fig. 1(a), the dark colours of blue, red, and green in Figs. 1 (b), (c), and (d) clearly show the difference. Here it should note that the scattering preference does not mean it is just this. For example, Huynen dichotomy prefers the symmetric and regular scatterers. This does not mean the extracted single targets from the dichotomy are all symmetric and regular. The actual scattering of target only depends on its Pauli vector. In this regarding, the preference of the dichotomy can only provide a direct and superficial description of scattering information. However, in the following we will show that for the purpose of visualization and classification this information is enough.

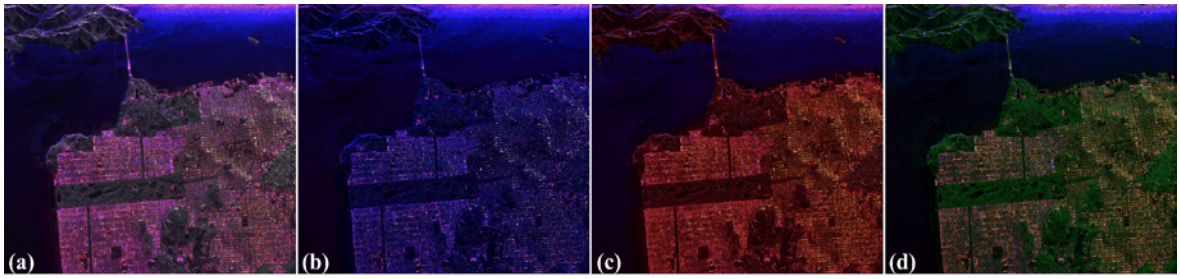

Figure 1: Pauli pseudo-colour display of (a) the original San Francisco data and (b-d) the extracted single targets from Huynen canonical dichotomy, where (b), (c), and (d) correspond to vectors $\vec{k}_1$, $\vec{k}_2$, and $\vec{k}_3$, respectively.

3 Fast PolSAR Data Visualization with Classification Based on Huynen Canonical Dichotomy

The SPAN image and Pauli image are the two widely-used visualizations of PolSAR data. But they only convey limited information contained in the coherence matrix of a random scatterer. Some recent works [5] have dedicated to visualize PolSAR information to the most. All of them added the scattering information and purity information of random target into SPAN image, a hue-saturation-intensity (HSI) presentation is thus obtained. The Cloude-Pottier entropy (*H*) and alpha parameters or their alternative are used as saturation and hue to show the randomness and scattering mechanism, while SPAN is used as intensity. Considering the valid scope of *Hue*, *Sat* and *Int*, some simple transformations are necessary. The following transformation is used in the PolSARPro:

$$\begin{cases} Hue = 4(90^\circ - \alpha) - 60 \\ Sat = 1 - H \\ Int = Normalzie(\log(SPAN)) \end{cases} . \qquad (2)$$

This paper is dedicated to develop a new PolSAR data visualization approach still based on HSI, but our *Hue* and *Sat* descriptions are from Huynen canonical dichotomy. The Pauli vectors from this decomposition are just the columns of [*T*], thus the complex eigendecomposition operation in Cloude-Pottier decomposition can be immediately avoided, and the resulted improvement of computation efficiency can be envisaged.

3.1 Scattering Degree of Preference and Application to Classification

The three target dichotomies prefer the sphere, dihedral, and volume scatterer, respectively, thus they can be used for classification. In order to measure the preference degree of each dichotomy, here we define a scattering degree of preference (*SDoP*) parameter

$$SDoP_i = \frac{SPAN_i}{SPAN} = \frac{\sum_{j=1}^{3} T_{ji}^2}{T_{ii}\sum_{j=1}^{3} T_{jj}}, i = 1,2,3 \qquad (3)$$

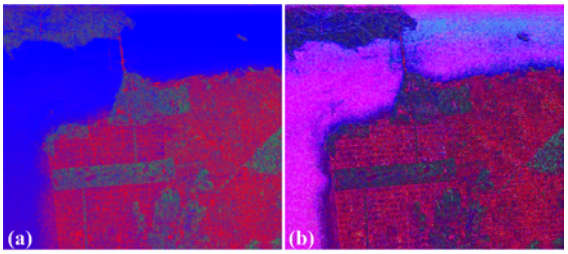

Figure 2: San Francisco data classification based on (a) scattering similarity and (b) scattering preference.

where $SPAN_i$ is the power of single target extracted from the *i*th dichotomy. *SPAN* in denominator is the power of random target. Thus *SDoP* measures the relative power and it is comparable to the wave degree of polarization (*WDoP*), which measures the relative power between the decomposed fully polarized wave and the original partially polarized wave. A simple classification of target can be achieved based on *SDoP*. For example, the scattering is labelled as "more preferable to irregular scatterer" if $SDoP_2$ is larger than $SDoP_1$ and $SDoP_3$. It is worthy to emphasize the "preferable" further here. In fact Chen *et al.* [4] has recently proposed to classify a random target into sphere (SS_1), dihedral (SS_2), and volume scatterer (SS_3) based on scattering similarity (*SS*):

$$SS_i = \frac{T_{ii}}{T_{11} + T_{22} + T_{33}}, i = 1,2,3 . \qquad (4)$$

They are in fact the normalized diagonal entries of [*T*] [5]. Fig. 2(b) shows the classification of San Francisco scene based on *SDoP*, in which the blue colour denotes more preferable to symmetric/regular scatterer, such as sphere; red means more preferable to irregular scatterer, such as dihedral; and green shows more preferable to non-symmetric target, such as volume scatterer. Fig. 2(a) shows the classification based on *SS*, where the blue, red, and green colours denote more similar to sphere, dihedral, and volume scatterer, respectively. By comparing the two classifications we can observe that more information is reflected by *SDoP*. Particularly in the sea area, the scattering influence from radar LOS variation has been clearly identified and classified, which can be even comparable to the H/A/alpha-Wishart classifier [2]. The inferiority of *SS* to *SDoP* is straightforward because

SS is in fact a special *SDoP*. For example, let $\vec{k}_2 = A[0, 1, 0]^T$, i.e. the dihedral is considered, and then *SDoP* degenerates to *SS*.

3.2 Scattering Hue

Although *SDoP* looks attractive, it cannot quantitatively measure the scattering mechanism. To achieve this here we propose a scattering hue (*SH*) by comparing among $SDoP_1$, $SDoP_2$, and $SDoP_3$. Two different versions of *SH* are developed, i.e. the smooth *SH* and the rugged *SH*:

$$SDoP_{\max} = \max(SDoP_1, SDoP_2, SDoP_3)$$
$$SDoP_{\min} = \min(SDoP_1, SDoP_2, SDoP_3)$$

$$SH_{smooth} = 60 \times \begin{cases} \dfrac{SDoP_3 - SDoP_1}{SDoP_{\max} - SDoP_{\min}}, & \text{if } \begin{cases} SDoP_2 = SDoP_{\max} \\ SDoP_1 < SDoP_{31} \end{cases} \\ \dfrac{SDoP_3 - SDoP_1}{SDoP_{\max} - SDoP_{\min}} + 6, & \text{if } \begin{cases} SDoP_2 = SDoP_{\max} \\ SDoP_3 \geq SDoP \end{cases} \\ \dfrac{SDoP_1 - SDoP_2}{SDoP_{\max} - SDoP_{\min}} + 2, & \text{if } SDoP_3 = SDoP_{\max} \\ \dfrac{SDoP_2 - SDoP_3}{SDoP_{\max} - SDoP_{\min}} + 4, & \text{if } SDoP_1 = SDoP_{\max} \end{cases} \quad (5)$$

$$SH_{rugged} = 60 \times \begin{cases} \dfrac{SDoP_1 - SDoP_3}{SDoP_{\max} - SDoP_{\min}}, & \text{if } \begin{cases} SDoP_2 = SDoP_{\max} \\ SDoP_1 \geq SDoP_3 \end{cases} \\ \dfrac{SDoP_1 - SDoP_3}{SDoP_{\max} - SDoP_{\min}} + 6, & \text{if } \begin{cases} SDoP_2 = SDoP_{\max} \\ SDoP_1 < SDoP_3 \end{cases} \\ \dfrac{SDoP_2 - SDoP_1}{SDoP_{\max} - SDoP_{\min}} + 2, & \text{if } SDoP_3 = SDoP_{\max} \\ \dfrac{SDoP_3 - SDoP_2}{SDoP_{\max} - SDoP_{\min}} + 4, & \text{if } SDoP_1 = SDoP_{\max} \end{cases}$$

The colour circles of the two *SH*s are illustrated in Figs. 3 (a) and (b). They are divided into six zones. Zones I and II compose the colour $Group_1$, as shown in Fig. 3. They have more preference to dihedral than sphere and volume scatterer because $SDoP_2$ is larger than $SDoP_1$ and $SDoP_3$ here. The red colour is mostly located within these zones so as to well indicate the scattering of buildings. The difference between Zones I and II depends on the comparison of $SDoP_1$ and $SDoP_3$. The sphere scattering has more preference in Zone I than the volume scattering. A smooth colour transition from red to purple (fusion of red and blue) can be observed in this zone with the increase of $SDoP_1$. In the limit when $SDoP_1$ equals $SDoP_2$, the colour completely changes to purple. Zone II prefers more to volume scattering than sphere. A smooth colour transition from red to yellow (fusion of red and green) can be observed in this zone with the increase of $SDoP_3$, and the colour changes to yellow when $SDoP_1$ equals $SDoP_2$. A smooth scattering-related colour transition is thus achieved in $Group_1$. Zones III and IV compose colour $Group_2$, which prefer more to dihedral. The remaining Zones V and VI compose $Group_3$, which indicate more preferable to the volume scattering. Detail analysis of these four zones is omitted here. We term the *SH* circle in Fig. 3(a) as the smooth *SH* because it can also achieve a smooth colour transition among the

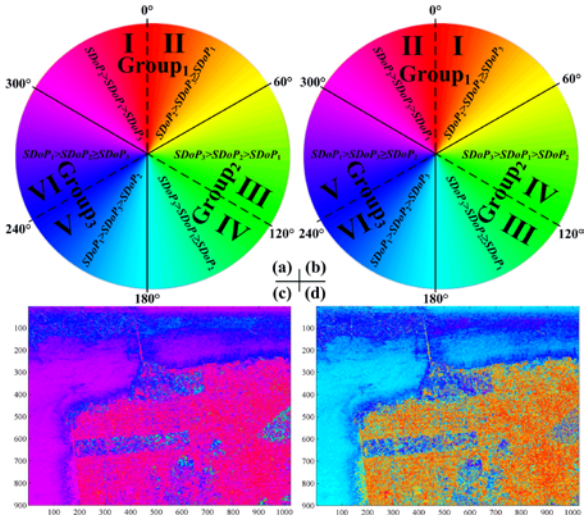

Figure 3: Colour circles of (a) smooth *SH* and (b) rugged *SH*, as well as the extracted (c) smooth *SH* and (d) rugged *SH* on San Francisco data.

three groups. Taking Zone I of $Group_1$ and Zone VI of $Group_3$ for example, these zones have the least preference to volume scatterer. However, Zone VI has more preference to sphere. The $SDoP_1$ and $SDoP_2$ values are comparable in the bordering area of these two zones, which infers the colour transition here should be smooth. The purple area around 300º in Fig. 3(a) just demonstrates this. The obtained smooth *SH* on San Francisco data is shown in Fig. 3(c), which not only contains the same scattering information as the *SDoP* classification in Fig. 2(b), but also shows the similar colouring. In Fig. 3(c), we can see much purple colour across the sea and city area, which means $SDoP_1$ and $SDoP_2$ are comparable there and $SDoP_3$ is the smallest. But in the practical remote sensing application, what we want mostly is not the least scattering but the dominant scattering mechanism, i.e. $SDoP_1$ is larger than $SDoP_2$, or $SDoP_2$ is larger than $SDoP_1$. In this regarding the smooth *SH* colour illustration cannot visually provide the information unless we check the original *SH* data. To solve this defect, we further develop a rugged *SH*, as shown in Fig. 3(b). The positions of Zones I and II, III and IV, V and VI are exchanged in this *SH* circle. Zone I is next to Zone VI in Fig. 3(a), but it is now 'opposite' to Zone VI. Thus the bordering colour ambiguity between them is resolved. Zone IV is now next to Zone I and it denotes the scattering preference of $SDoP_3 > SDoP_1 > SDoP_2$, being completely inverse to Zone I of $SDoP_2 > SDoP_1 > SDoP_3$. The bordering colour ambiguity in this case is greatly suppressed. The same changes also take on other five zones. The rugged *SH* of San Francisco data is shown in Fig. 3(d), which is much colourful than Fig. 3(c). More important, the purple colour in the sea and city area in Fig. 3(c) is now coloured as cyan and orange, which denotes more preferable to sphere and more preferable to dihedral, respectively. This is in accord with the ground truth. Thus the rugged *SH* is more competent to visualize the scattering mechanism.

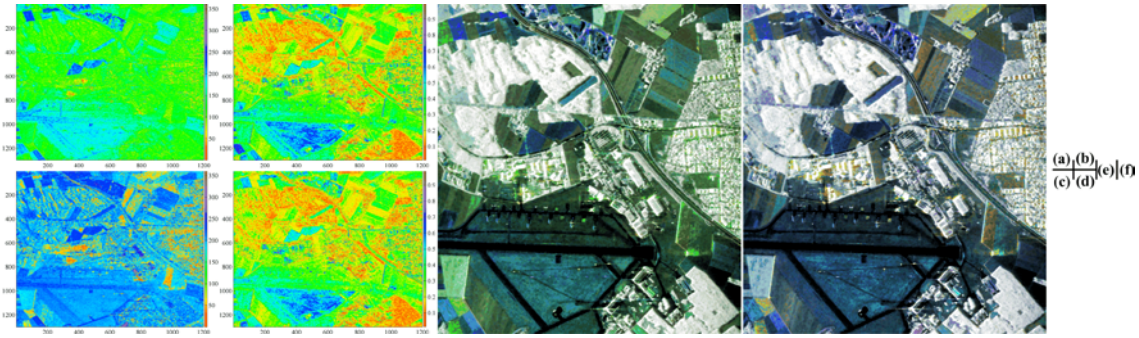

Figure 4: The (a) hue, (b) saturation, and (e) HSI visualization of Oberpfaffenhofen data based on H/alpha, as well as the (c) rugged *SH*, (d) *SS*, and (f) HSI visualization of the data based on Huynen canonical dichotomy.

Next we give a simple comparison between H/alpha hue and *SH*. To well illustrate the difference, DLR ESAR Oberpfaffenhofen data is selected, which shows a more complex scattering scene including forest, runway, bare land, vegetation land, and buildings. Figs. 4 (a) and (c) display alpha hue and *SH*, respectively. *SH*'s superiority over alpha hue on visualization of different scattering mechanism can be clearly observed. Thus we think *SH* can be a competent alternative to scattering alpha.

3.3 Scattering Saturation

SDoP denotes the relative power of the extracted single target with respect to that of the original random target, as defined in (3). We can easily find that *SDoP* achieves its maximum value of one when the original target is fully determined. On the other hand, if the target is partially determined or random, *SDoP* ranges from zero to one. Thus *SDoP* may also indicate target randomness or purity, just like *WDoP* to measure the depolarization of wave. Section 2 shows that the canonical dichotomy can independently extract three single targets with different scattering preference. This on the other hand may also show that the extracted three single targets can probably provide three different and independent understandings of the ensemble scatterer. Thus a statistical model can be obtained with the pseudo-probability as shown in (6). Then a mean estimation of *SDoP* is achieved:

$$\begin{cases} P_i = \dfrac{SPAN_i}{\sum_{j=1}^{3} SPAN_j}, i = 1,2,3 \\ \overline{SDoP} = \sum_{j=1}^{3} P_j \cdot SDoP_j = \dfrac{\sum_{j=1}^{3} SPAN_j^2}{SPAN \sum_{j=1}^{3} SPAN_j}. \\ SS = \dfrac{3}{2}\overline{SDoP} - \dfrac{1}{2} \end{cases} \quad (6)$$

The mean is one for the determined target, is 1/3 for the random noisy target, and is between for the distributed target. Thus it can measure the scattering randomness and be used as saturation just like the scattering entropy. A scattering saturation (*SS*) parameter is developed by simply transforming the average *SDoP* so as to keep the saturation within the interval of [0, 1]. Figs. 4 (b) and (d) show the *H*/alpha-based saturation and *SS*, respectively. We can see that they behave nearly the same. The detail comparison is passed over here due to space limitation.

3.4 HSI Visualization

By integrating *SH*, *SS*, and *SPAN*, the final HSI illustration is obtained and shown in Fig. 4(f). Fig. 4(e) further displays the result obtained from H/alpha. The scattering details in Fig. 4(e) can all be clearly observed in Fig. 4(f). But Fig. 4(f) looks better than Fig. 4(e) on differentiation of scattering mechanism. This mainly lies in the superiority of *SH*. The visualization elements *SH* and *SS* can be directly obtained without any eigendecomposition, thus the efficiency improvement is considerable.

4 Conclusions

Huynen decomposition is used for fast PolSAR data visualization and classification. The visualization is comparable and even better than that based on H/alpha, besides the high efficiency. The classification is much better than that based on *SS* because of the power of *SDoP*, from which we not only can obtain *SH* to show the scattering mechanism, but also can obtain *SS* to describe the scattering randomness. *SH* and *SS* perform comparable to and even better than the scattering alpha and entropy.

References

[1] J. R. Huynen: *Phenomenological Theory of Radar Targets*, Tech. Univ. Delft, 1970.

[2] J.-S. Lee and E. Pottier: *Polarimetric Radar Imaging: From Basics to Applications*, CRC Press, 2009.

[3] D. Li and Y. Zhang: *Huynen Dichotomy-based Radar Target Adaptive Extraction*, Proc. PIERS, pp. 881-885, 2013.

[4] Q. Chen *et al.*: *IEEE TGRS*, vol. 51, no. 3, pp. 1817-1825, 2013.

[5] J. Praks, E. C. Koeniguer, and M. T. Hallikainen: *IEEE TGRS*, vol. 47, no. 7, pp. 2262-2274, 2009.